Regular Article

Growth competition during columnar solidification of seaweed microstructures*

Insights from 3-D phase-field simulations

Kumar Ankit^{1,a} and Martin E. Glicksman²

- School for Engineering of Matter, Transport and Energy, Arizona State University, 551 E. Tyler Mall, Tempe, AZ 85287, USA
- Florida Institute of Technology, Allen S. Henry Chair and University Professor, 150 W. University Blvd., Melbourne, FL 32955, USA

Received 2 June 2019 and Received in final form 3 January 2020

Published online: 25 February 2020

© EDP Sciences / Società Italiana di Fisica / Springer-Verlag GmbH Germany, part of Springer Nature,

Abstract. The mechanisms by which interfacial instabilities instigate the growth of solidification patterns is a topic of longstanding interest. In columnar solidification of metallic melts, where the solid-liquid interfacial energy is anisotropic, evolving dendritic patterns compete depending on their relative misorientation. By contrast, organic "plastic crystals", such as alloys based on succinonitrile, where the anisotropy in their solid-liquid interfacial energy is extremely weak, solidify forming seaweed patterns that typically exhibit little, if any, growth competition. We explore in this study mechanisms by which columnar solidification microstructures of binary alloys with low crystalline anisotropy compete. We adopt toward this end a validated Navier-Stokes multiphase-field approach to characterize the influence of grain misorientation, seed morphology, and melt advection on the growth competition. Simulated seaweed patterns indicate profound influences of all three factors, although characteristic solidification morphologies are observed to evolve depending on the melt flow intensity.

1 Introduction

Theoretical criteria for the linear instability of a planar interface were first derived by Mullins and Sekerka [1], who proposed that the stability of monocrystalline solid/liquid interfaces during solidification is governed by the interfacial wavelength of the perturbation and the extent of constitutional supercooling. However, when a polycrystal is in contact with its melt, the solidification front is replete with grain boundary grooves (GBGs) that can initiate instabilities due to redistribution of solute near the solid-liquid interface. Several experimental studies [2–7] on directional solidification of weakly anisotropic organic crystals, such as succinonitrile (SCN) and its derivative alloys reported morphological instability at GBGs, characterized by amplification of adjacent humps projecting into the melt. If the melt is supercooled, humps adjacent to GBGs amplify and often compete to outgrow each other. In the presence of anisotropy of the solid-liquid interfacial energy, amplifying humps evolve into dendrites and the ensuing growth

competition is governed by the relative misorientation of grains. Therefore, it can be expected that when the surface energy is isotropic, or weakly anisotropic, the solidifying patterns which manifest as "seaweed" will *not* compete with one another. Monocrystalline dendritic and seaweed patterns simulated using the phase-field technique are shown in fig. 1. This study uses phase-field simulations

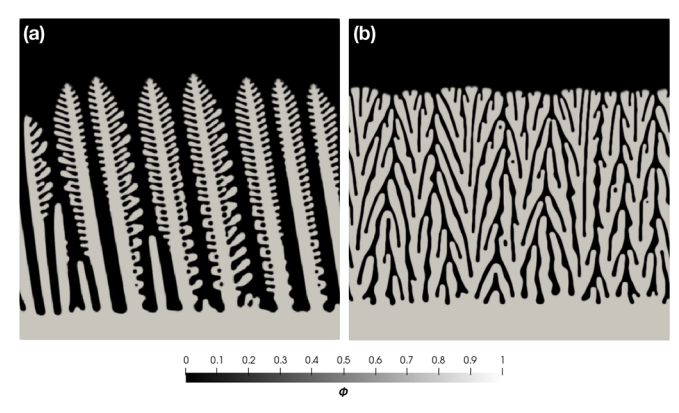


Fig. 1. Evolution of columnar (a) dendrites and (b) seaweed microstructures simulated using the phase-field model outlined in sect. 3.

 $^{^{\}star}$ Contribution to the Topical Issue "Branching Dynamics at the Mesoscopic Scale", edited by Yongsheng Han, Hui Xing, Dongke Sun.

a e-mail: kumar.ankit@asu.edu

to demonstrate, for the first time, that growth competition can occur during columnar solidification of binary alloys even when the corresponding surface energy is isotropic. The following article provides an overview of the conditions which favor growth competition during the solidification of seaweed-like microstructures.

2 Background

The mechanism by which grain boundary groove instabilities instigate pattern formation was first shown by Schaefer and Glicksman [4]. Those investigators observed that as the initial ridges adjacent to a GBG amplified, pairs of parallel secondary ridges appeared beside them. The primary ridges then progressively broke their two-dimensional symmetry into periodic rows of threedimensional hillocks and knobs, some of which eventually evolved into dendrites. Similarly, in situ experiments by Noël et al. [2] and Xing et al. [3] showed that the formation of GBGs led to the nucleation of ridges and depressions over the seed surface. This mechanism has recently been verified in computational studies of surface rippling [8]. If the surface energy is anisotropic, then the alignment of evolving dendrites corresponds epitaxially to the orientation of their parent grains. Although the ensuing growth competition is known to be governed by the relative misorientation among the neighboring grains [9], melt convection can inhibit the growth of seaweed patterns downstream, resulting in localized growth [5, 7, 6, 10, 11].

In weakly anisotropic crystals, a pattern's extending tips —unlike the behavior observed in needle-like dendrites— splits repeatedly, forming seaweed structures [12–17]. Evolution of such patterns in isotropic systems has been extensively studied in directional solidification experiments [17,18] and by computation [19]. However, studies on growth competition involving columnar solidification of seaweed microstructures have, heretofore, not been reported. The following questions arise: If melt convection can suppress growth of seaweed patterns downstream, can this interaction also induce growth competition? What are the characteristics of solidification microstructures that form when weakly anisotropic crystals compete? Beyond melt convection, what other factors induce growth competition in seaweed structures? In order to address these questions, we employ a phase-field method [20–26,9,8] that has been extensively applied to the study of material and process parameters on the evolution of solidification microstructures.

In sect. 3, we formulate the phase-field model, where melt convection is introduced in a manner similar to Beckermann's model [27]. The phase-field and flow solver are validated in sect. 4 with calculation of a drag coefficient, C_d , for cross-flow at several Reynolds numbers, Re, around an infinite cylinder. In sect. 5.1, we report simulations of non-competing seaweed evolution in three dimensions. In the following sections, we explore the influence of grain morphology, misorientation, and flow intensity, that induce anisotropic evolution and growth competition. Section 6 concludes and summarizes our findings.

3 Method

It is well known that the presence of convection in the liquid phase can lead to the formation of diverse microstructures [21,28–30,20]. In the present work, we reformulate the grand-potential model [31] by incorporating the convective term similar to a previous study of Beckermann [27]. The evolution of the phases is determined by the minimization of the modified functional $\mathrm{d}\Omega/\mathrm{d}t\leqslant 0$, given by

$$\Omega(T, \boldsymbol{\mu}, \boldsymbol{\phi}) = \int_{\Omega} \left[\Psi(T, \boldsymbol{\mu}, \boldsymbol{\phi}) + \left(\epsilon a(\boldsymbol{\phi}, \nabla \boldsymbol{\phi}) + \frac{1}{\epsilon} w(\boldsymbol{\phi}) \right) \right] d\Omega.$$
(1)

Here, T is the temperature, $\mu = (\mu_i, \dots, \mu_{K-1})$ is a vector consisting of K-1 chemical potentials of the system at a given temperature and $\phi = (\phi_{\alpha}, \dots, \phi_{N})$ describes the phase index vector with ϕ_{α} being the local volume fraction of the α phase. ϵ is a length scale related to the thickness of the diffuse interface, while $\epsilon a(\phi, \nabla \phi)$ and $\frac{1}{\epsilon}w(\phi)$ are the gradient- and obstacle-type energy densities taking into account the thermodynamics of the interface, respectively [32]. The grand-potential density, $\Psi(T, \mu, \phi)$, is the Legendre transform of the free energy density of the system $f(T, \mathbf{c}, \phi)$, expressed as the interpolation of individual grand-potential densities Ψ_{α}

$$\Psi(T, \boldsymbol{\mu}, \boldsymbol{\phi}) = \sum_{\alpha=1}^{N} \Psi_{\alpha}(T, \boldsymbol{\mu}) h(\phi_{\alpha}), \tag{2}$$

with

$$\Psi_{\alpha}(T, \boldsymbol{\mu}) = f_{\alpha}(\boldsymbol{c}^{\alpha}(\boldsymbol{\mu}, T), T) - \sum_{i=1}^{K-1} \mu_{i} c_{i}^{\alpha}(\boldsymbol{\mu}, T). \quad (3)$$

For a multiphase-field representation, $h(\phi_{\alpha})$ is an interpolation function of the form

$$h(\phi_{\alpha}) = \frac{\tilde{h}(\phi_{\alpha})}{\sum_{\beta} \tilde{h}(\phi_{\beta})}, \tag{4}$$

which ensures that the condition $\sum_{\beta} h(\phi_{\beta}) = 1$ is always fulfilled [33]. $\tilde{h}(\phi_{\alpha})$ is expressed as

$$\tilde{h}(\phi_{\alpha}) = \phi_{\alpha}^2 (3 - 2\phi_{\alpha}). \tag{5}$$

The free energy of an isothermal binary alloy system is described by the following polynomial:

$$f_{\alpha}(c_A, c_B) = A^{\alpha} c_A^2 + B^{\alpha} c_B^2 + D^{\alpha} c_A + E^{\alpha} c_B + F^{\alpha}.$$
 (6)

Here, c_A and c_B are the mole concentrations of A and B components, respectively. A^{α} , B^{α} , D^{α} , E^{α} , F^{α} represent the fitted coefficients. Because of the local constraint $c_A + c_B = 1$, we rewrite the above equation in terms of c_A as

$$f_{\alpha}(c_{A}) = (A^{\alpha} + B^{\alpha})c_{A}^{2} + (D^{\alpha} - E^{\alpha} - 2B^{\alpha})c_{A} + E^{\alpha} + F^{\alpha} + B^{\alpha},$$
(7)

which is formulated as

$$f_{\alpha}(c_A) = O^{\alpha} c_A^2 + N^{\alpha} c_A + P^{\alpha}, \tag{8}$$

Table 1. Parameters used in our phase-field simulations.

Description	Parameter	Value
Free energy coefficients	O^{α}	1.00
	N^{lpha}	-0.40
	P^{lpha}	0.04
	O^{eta}	2.00
	N^{eta}	-3.20
	P^{eta}	1.28
Discretized grid space	$\Delta x = \Delta z$	1.00
Melt supersaturation	$s = \left(\frac{c_B^{\beta, \mathrm{eq}} - c_B^{\beta}}{c_B^{\beta, \mathrm{eq}} - c_B^{\alpha, \mathrm{eq}}}\right)$	0.50
Diffusion coefficients	$D_A^\beta = D_B^\beta$	1.00
Third-order term (eq. (11))	$\gamma_{lphaeta\delta}$	10.00
Interface width	ϵ	4.00
Relaxation constant	au	1.28
Fluid density	ho	1.00
Dynamic viscosity	η	1.00
Kinematic viscosity	u	1.00
Ratio $r_0 = \left(\frac{\sigma_{sl}}{\sigma_{qb}}\right)$	r_0	0.5, 0.7
Safety factor (eq. (26))	ζ	0.20

where, $O^{\alpha} = A^{\alpha} + B^{\alpha}$, $N^{\alpha} = D^{\alpha} - E^{\alpha} - 2B^{\alpha}$ and $P^{\alpha} = E^{\alpha} + B^{\alpha} + F^{\alpha}$. From $\mu = \partial_{c_A} f^{\alpha} = \mu(c_A)$ and $c_A(\mu) = (\mu - N^{\alpha})/2O^{\alpha}$, the corresponding grand-potential densities were calculated in a method described by Choudhury [25]. The coefficients O^{α} , N^{α} and P^{α} are determined using the free energy densities, chemical potential as well as the equilibrium mole fractions for a model system. Moreover, the present work can be extended to analyze solidification of any binary alloy [34, 23, 19, 35]. Here, the mole fractions of component B in the solid α and the liquid β are set as $c_B^{\alpha, \rm eq} = 0.2$ and $c_B^{\beta, \rm eq} = 0.8$, respectively. We emphasize that the instabilities originating at grain boundaries, which we simulate using this model, are not affected by the selected mole fractions and the parabolic free energies. Rather, the evolution of a non-planar structure depends on the melt supersaturation $s=(c_B^{\beta,\mathrm{eq}}-c_B^{\beta})/(c_B^{\beta,\mathrm{eq}}-c_B^{\alpha,\mathrm{eq}})$, where c_B^{β} is the initial concentration in liquid phase. Furthermore, the free energy coefficients, equilibrium concentrations and the melt supersaturation in table 1 are alloy-specific. All the numerical parameters used in our simulations are given in table 1. The simulation time is normalized by l_0^2/D^l , where $l_0 = \sigma/(RT/v_m)$ is the capillary length, R is the gas constant, σ represents interfacial energy and v_m is the molar

The gradient- and the obstacle-type energy densities in eq. (1) are expressed as

$$\epsilon a(\phi, \nabla \phi) = \epsilon \sum_{\alpha, \beta = 1}^{N, N} \sigma_{\alpha \beta} [a_c(q_{\alpha \beta})^2] |q_{\alpha \beta}|^2, \qquad (9)$$

where $q_{\alpha\beta}$ models the surface energy anisotropy of the evolving phase boundary, $\sigma_{\alpha\beta}$ is the interfacial free energy per unit area of the α/β phase boundary. The physics of each phase is distinguished via the generalized antisymmetric gradient vector $q_{\alpha\beta}$ of the form $q_{\alpha\beta} = \phi_{\alpha}\nabla\phi_{\beta} - \phi_{\beta}\nabla\phi_{\alpha}$. The isotropic surface energy is postulated in our model via $a_c(q_{\alpha\beta}) = 1$ for a typical seaweed growth. The multiobstacle-type potential is of the form

$$\frac{1}{\epsilon}w(\phi) = \frac{1}{\epsilon} \frac{16}{\pi^2} \sum_{\alpha < \beta} \sigma_{\alpha\beta} \phi_{\alpha} \phi_{\beta} + \sum_{\alpha < \beta < \delta} \gamma_{\alpha\beta\delta} \phi_{\alpha} \phi_{\beta} \phi_{\delta}. \quad (10)$$

In order to avoid third-phase contributions in a two-phase interface, additional third-order terms $\sim \phi_\alpha \phi_\alpha \phi_\delta$ are added to the multiobstacle potential [32]. The presence of spurious and artificial phases increases the potential in the two-phase region and thereby becomes unfavorable. The analytics and numerical handling of this term has been discussed previously by Hötzer [36]. The parameter $\gamma_{\alpha\beta\delta}$ in the above equation is chosen such that it satisfies the condition

$$\gamma_{\alpha\beta\delta} \geqslant \frac{96\sigma_{ij}}{\pi^2}, (i,j) \in \{(\alpha,\beta), (\beta,\delta), (\delta,\alpha)\}.$$
(11)

The evolution equation for N phase-field variables is written as

$$\tau \epsilon \frac{\partial \phi_{\alpha}}{\partial t} = \epsilon \left(\nabla \cdot \frac{\partial a(\phi, \nabla \phi)}{\partial \nabla \phi_{\alpha}} - \frac{\partial a(\phi, \nabla \phi)}{\partial \phi_{\alpha}} \right) - \frac{1}{\epsilon} \frac{\partial w(\phi)}{\partial \phi_{\alpha}} - \frac{\partial \Psi(T, \mu, \phi)}{\partial \phi_{\alpha}} - \Gamma,$$
(12)

where Γ is a Lagrange multiplier so that the local constraint $\sum_{\alpha=1}^{N} \phi_{\alpha} = 1$ is fulfilled. The relaxation constant τ is chosen according to the expression in [31], such that the kinetics at the interface vanishes. The evolution equation for the concentration fields can be written as

$$\frac{\partial c_i}{\partial t} = \nabla \cdot \left(\sum_{i=1}^{K-1} M_{ij}(\phi) \nabla \mu_j \right). \tag{13}$$

The term $M_{ij}(\phi)$ represents mobilities of the interface, which are interpolated by the individual phases as

$$M_{ij}(\boldsymbol{\phi}) = \sum_{\alpha=1}^{N-1} M_{ij}^{\alpha} h(\phi_{\alpha}), \tag{14}$$

where phase mobilities M_{ij}^{α} are expressed as

$$M_{ij}^{\alpha} = D_{ij}^{\alpha} \frac{\partial c_i^{\alpha}(\boldsymbol{\mu}, T)}{\partial \mu_j}.$$
 (15)

In order to incorporate melt convection in our phasefield model, the convective term is coupled with the evolution equation for the chemical potentials. Henceforth, let us first begin with the following constraint [31]:

$$c_i = \sum_{\alpha=1}^{N} c_i^{\alpha}(\boldsymbol{\mu}, T) h(\phi_{\alpha}). \tag{16}$$

Now, rewriting the above equation through the time derivative of the concentration fields gives us

$$\frac{\partial c_i}{\partial t} = \sum_{\alpha=1}^{N} \frac{\partial c_i^{\alpha}(\boldsymbol{\mu})}{\partial \mu} \frac{\partial \mu}{\partial t} h(\phi_{\alpha}) + c_i^{\alpha}(\boldsymbol{\mu}) h'(\phi_{\alpha}) \frac{\partial \phi}{\partial t} . \tag{17}$$

Therefore, the evolution equation for K-1 independent chemical potentials can be obtained by substituting the above equation in eq. (13)

$$\sum_{\alpha=1}^{N} \frac{\partial c_{i}^{\alpha}(\boldsymbol{\mu})}{\partial \mu_{j}} \frac{\partial \mu}{\partial t} h(\phi_{\alpha}) + c_{i}^{\alpha}(\boldsymbol{\mu}) h'(\phi_{\alpha}) \frac{\partial \phi}{\partial t} =$$

$$\nabla \cdot \left(\sum_{j=1}^{K-1} M_{ij}(\boldsymbol{\phi}) \nabla \mu_{j} - (\boldsymbol{u}c_{i}) - \boldsymbol{J}_{at} - \boldsymbol{q} \right).$$
(18)

Rearranging the terms we get

$$\frac{\partial \mu}{\partial t} = \sum_{i,j=1}^{K-1} \left[\sum_{\alpha=1}^{N} h(\phi_{\alpha}) \frac{\partial c_{i}^{\alpha}(\boldsymbol{\mu})}{\partial \mu_{j}} \right]_{ij}^{-1} \\
\times \left\{ \nabla \cdot \sum_{i,j=1}^{K-1} \left(M_{ij}(\boldsymbol{\phi}) \nabla \mu_{j} - \boldsymbol{u} c_{i} - \boldsymbol{J}_{at} - \boldsymbol{q} \right) \right. \\
\left. - c_{i}^{\alpha}(\boldsymbol{\mu}) h'(\phi_{\alpha}) \frac{\partial \phi}{\partial t} \right\}. \tag{19}$$

The mass flux on the right-hand side has contributions from diffusion as a result of gradients in the chemical potential, the interface mobility $M_{ij}(\phi)$ is defined in eq. (15) and u is the liquid velocity. J_{at} represents the antitrapping current that produces a mass flux along the normal direction, and thereby counterbalances the trapping current due to the presence of non-equilibrium artifacts such as the solute trapping [31], expressed as

$$J_{at} = -\frac{\pi \epsilon}{4} \frac{g(\phi_{\alpha})[1 - h(\phi_{\alpha})]}{\sqrt{\phi_{\alpha}(1 - \phi_{\alpha})}} \times \left[c^{\beta}(\boldsymbol{\mu}, T) - c^{\alpha}(\boldsymbol{\mu}, T)\right] \frac{\partial \phi_{\alpha}}{\partial t} \frac{\nabla \phi_{\alpha}}{|\nabla \phi_{\alpha}|}.$$
 (20)

The noise term "q" in eq. (19) is introduced to account for thermal fluctuations in our simulations. Through the fluctuation-dissipation theorem [37,38], q follows a Gaussian distribution with a variance $\langle q_m(x,t)q_n(x',t)\rangle = 2D_B^\beta F_u \delta_{mn} \delta(x-x')\delta(t-t')$. Here δ is the Dirac function, δ_{mn} is the Kronecker delta, q_n , is the random variable along the normal direction, while q_m , with m=x,z, are the generated random variables in space and time, respectively, through the conventional Polar Marsaglia method [39]. The imposed noise amplitude $F_u=0.06$ is calculated according to Karma and Rappel [38].

In the present two-phase study, we introduce the non-conserved quantity ϕ_{β} for the liquid phase and ϕ_{α} for solid, $\phi_{\alpha} = 1 - \phi_{\beta}$, on the basis of the local constraint $\sum_{\alpha=1}^{N} \phi_{\alpha} = 1$. The derivation of the Navier-Stokes equation as a function of the phase-field vector ϕ is similar

to Beckermann [27]. Such a formulation is usually done for simulations under the influence of melt convection [40, 41]. The velocity of the rigid and stationary solid phase ϕ_{α} is assumed to be zero $(\phi_{\alpha} u_{\alpha} = 0)$. Hence, the velocity vector \boldsymbol{u} is denoted as $\phi_{\beta} u_{\beta}$, since $\boldsymbol{u} = \phi_{\alpha} u_{\alpha} + \phi_{\beta} u_{\beta}$ and $\phi_{\alpha} u_{\alpha} = 0$. Thereby, the convective term in eq. (19) reads

$$\nabla \cdot (\phi_{\beta} \boldsymbol{u}_{\beta} c_i) = c_i \nabla \cdot (\phi_{\beta} \boldsymbol{u}_{\beta}) + \phi_{\beta} \boldsymbol{u}_{\beta} \cdot \nabla c_i, \qquad (21)$$

where

$$\nabla \cdot (\phi_{\beta} \boldsymbol{u}_{\beta}) = 0, \tag{22}$$

is the incompressibility condition. Therefore, eq. (19) for a binary variant can be rewritten as

$$\frac{\partial \mu}{\partial t} = \sum_{i,j=1}^{K-1} \left[\sum_{\alpha=1}^{N} h(\phi_{\alpha}) \frac{\partial c_{i}^{\alpha}(\boldsymbol{\mu})}{\partial \mu_{j}} \right]_{ij}^{-1} \\
\times \left\{ \nabla \cdot (M \nabla \mu_{i}) - \phi_{\beta} \boldsymbol{u}_{\beta} \cdot \nabla c_{i} \right. \\
\left. - \nabla \cdot (\boldsymbol{J}_{at} + \boldsymbol{q}) - c_{i}^{\alpha}(\boldsymbol{\mu}) h'(\phi_{\alpha}) \frac{\partial \phi}{\partial t} \right\}. \tag{23}$$

Furthermore, the Navier-Stokes equation is given as

$$\rho \left(\partial_t (\phi_{\beta} \boldsymbol{u}_{\beta}) + \phi_{\beta} \boldsymbol{u}_{\beta} \cdot \nabla \boldsymbol{u}_{\beta} \right) = \\ -\nabla p + \nabla \cdot \left[\eta \left(\nabla \phi_{\beta} \boldsymbol{u}_{\beta} + \nabla \phi_{\beta} \boldsymbol{u}_{\beta}^T \right) \right] - \boldsymbol{M}_l^d, \tag{24}$$

where ρ , $\phi_{\beta} \boldsymbol{u}_{\beta}$, p, η denote the density, velocity vector, pressure and the dynamic viscosity of the liquid, respectively. The last term, \boldsymbol{M}_{l}^{d} , on the right-hand side encapsulates the dissipative viscous stress [27], expressed as

$$\mathbf{M}_{l}^{d} = \eta h \phi \frac{\mathbf{u}}{\epsilon} |\nabla \phi_{\beta}|, \tag{25}$$

where, h is the dimensionless parameter which provides a distributed momentum sink in the diffuse interface region, thus forcing the liquid velocity to zero as $\phi \to 1$. The discontinuity of the flow velocity across the solid-liquid interface is addressed via performing an asymptotic analysis, i.e., matching the inner and outer solution of the velocity profile across the diffuse interface. A no-slip condition is applied at the solid-liquid interface $\phi = 0.5$ and thereby, the velocity vector \boldsymbol{u} varies linearly across the diffuse interface. Independent of the imposed pressure gradient, the dissipative term plays a fundamental role in smoothing the velocity profile regardless of the diffuse interface thickness ϵ . In the present model, h has the value 7.989 for the obstacle-type potential eq. (10) [42].

To summarize, eqs. (22), (23), and (24) incorporate the liquid phase convection in our grand-potential formulation [31]. The above equations are solved using a finite discretization on a staggered mesh. The time derivative follows an explicit Euler scheme. In order to perform a numerically stable algorithm while avoiding oscillations, the time step is restricted via the following condition [43]:

$$\Delta t < \zeta \min\left(\frac{Re}{2}\left(\frac{\nu}{\Delta x^2} + \frac{\nu}{\Delta z^2}\right)^{-1}, \frac{\Delta x}{|u_{max}|}, \frac{\Delta z}{|w_{max}|}\right),$$
(26)

where, $Re = \frac{\rho uL}{\eta}$. Here, L represents the dimensionless characteristic length, and u is the absolute value of the velocity vector and ν is the kinematic viscosity of the fluid. ζ is a safety factor, Δx , Δz are the discretized spatial steps in x and z dimensions, respectively and u_{max} and w_{max} are the maximal values of the velocities in the x and z directions, respectively. The current numerical algorithm is implemented through a C program which is parallelized via message passing interface (MPI).

4 Validation

4.1 Dihedral angle

To validate Young's law using the phase-field model described above, we chose an initial system condition comprised, respectively, of two grains, each of width and thickness, $2000\Delta x$ and $100\Delta x$. No-flux boundary conditions are assigned on the left- and right-hand edges of the numerical domain. The GBG's dihedral angle, ω_d , which corresponds to local equilibrium at the point where interfacial tensions balance, is given by

$$\omega_d = 2\cos^{-1}\left(\frac{\sigma_{gb}}{2\sigma_{s\ell}}\right),\tag{27}$$

where the grain boundary energy, σ_{gb} , and the solid-liquid interfacial energy, $\sigma_{s\ell}$, can be analytically derived [44,45]. For simplicity, we assume that *all* energies are isotropic, and, specifically, that the solid-liquid interfacial energies along both grains remains constant and equal. In accordance with eq. (27), figs. 2(a), (b), (c) show progressively that the simulated equilibrium dihedral angle decreases with increasing grain boundary energy.

4.2 Grooving kinetics: Mullins theory

Mullins showed [46] that the groove depth, d_g , relates to time, t, as

$$\frac{d_g}{d_0} = \left(\frac{t}{t_0}\right)^n. \tag{28}$$

where, d_0 and t_0 are parameters used for nondimensionalization of length and time scales while the power-law exponent n equals $\frac{1}{3}$ for volume-diffusioncontrolled grooving. In order to validate our phase-field model, we chose the same initial conditions as specified in sect. 4.1. A representative snapshot corresponding to a dihedral angle of $\omega_d = 120^\circ$, where $\sigma_{gb} = \sigma_{s\ell}$, is shown in the upper-left inset in fig. 2(d). The temporal variation of groove depth, d_g , is found to obey a power-law scaling exponent of n = 0.332, which is in good agreement with the prediction of Mullins theory.

4.3 Drag coefficient

We validate our solution of the Navier-Stokes equation (24) through the calculation of the drag coefficient

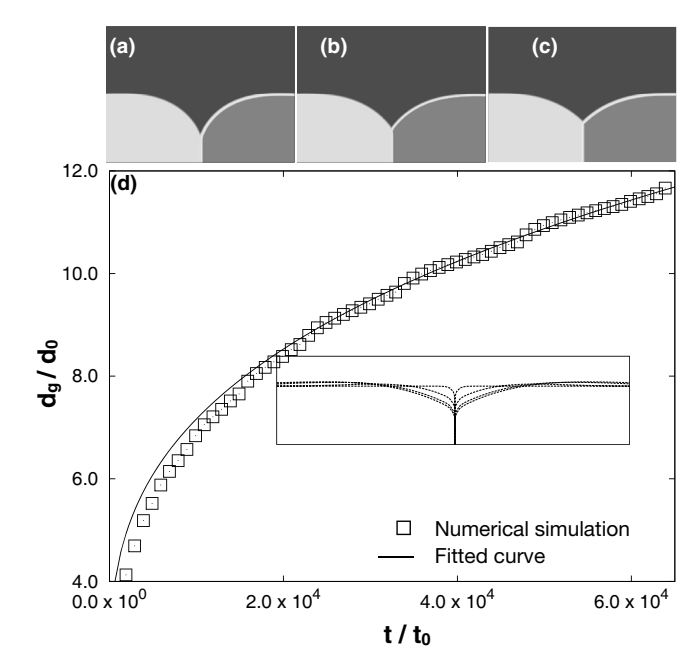


Fig. 2. Simulations of isotropic grain boundary grooves: (a) $\sigma_{s,l} = 0.5\sigma_{gb}$, (b) $\sigma_{s,l} = 0.6\sigma_{gb}$, and (c) $\sigma_{s,l} = 0.7\sigma_{gb}$. The illustrated snapshots of the groove region correspond to a numerical domain size of $2000\Delta x \times 200\Delta x$, with no-flux boundary conditions on the left and right edges. (d) Comparison of Mullins theory with numerically simulated grain boundary grooving kinetics for volume-diffusion—controlled regime. Data points represent the normalized groove depth whereas the curved line is a power-law fit (growth exponent, n=0.332). Temporal grooving is shown in the inset.

for a circular cylinder for a range of Reynolds numbers (Re), as shown in fig. 3. The drag coefficient (C_d) is a dimensionless quantity which quantifies the amount of drag force experienced by a body submerged in a fluid. It is expressed as

$$C_d = \frac{F}{\frac{1}{2}u^2\rho A},\tag{29}$$

where F is the magnitude of the drag force experienced by a body due to the combined influence of frictional effects and pressure gradients acting parallel to the flow direction, and A represents the projected area of the body in the direction of the flow. The schematic diagram in the inset of fig. 3 shows a two-dimensional domain box considered for the flow simulations. The square domain contains 500×500 cells in x and z dimensions, where $\Delta x = \Delta z = 1.0$ is the size of each grid. The position of a $20\Delta x$ diameter cylinder is chosen such that the axis is at the center of the x-z plane. For influx, a uniform fluid velocity is introduced at x = 0 while outflow occurs at x = 500 where the gradient of velocity in the x-direction is zero. The slip boundary conditions are chosen for the top and bottom boundaries, i.e., at z = 0 and z = 500, respectively, so that the frictional losses are negated. The plot shown in fig. 3 depicts the drag coefficient at various Re. In accordance with eq. (29), the drag coefficient decreases with an increase in Re. The present validation is

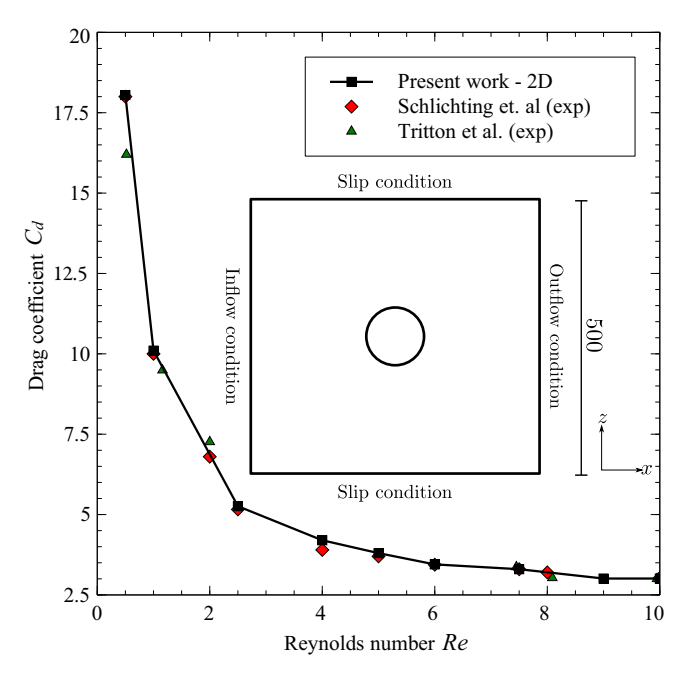


Fig. 3. The inset shows a simulation box with a domain size of 500×500 cells selected for the calculation of the drag coefficient, C_d . At the center of the x-z plane a two-dimensional cylinder with a diameter of $20\Delta x$ is chosen. For inflow, a uniform velocity is imposed at z=0. In order to avoid frictional loss at the boundaries, a slip boundary condition is applied at z=0 and z=500. The drag coefficient plotted as a function of the Reynolds number (Re) in two and three dimensions for a circular cylinder agrees favorably with previous studies [47,48].

in favorable agreement with previous studies, where the drag coefficient was calculated for a circular [47] and for an infinite cylinder [48]. A detailed study on the application of this model on the convection-mediated growth competition in seaweed microstructures has recently been reported by one of the authors [42].

5 Results

5.1 Isotropic patterns

The surface of a polycrystalline pure material in contact with its melt is composed of grain boundary groove roots and pits that can instigate morphological instabilities during solidification. If the melt is supersaturated, such instabilities are characterized by rippling of the surface adjacent to the grooves, followed by their temporal amplification, as shown in previous experimental [4,2,5,3] and simulation [8] studies. As a step towards understanding how GBGs impact the ensuing pattern formation, we studied the evolution of seaweed-like structures to explore the influences of surface energy, grain misorientation, and melt convection.

To test the accuracy of this model, we simulated the two- and the three-dimensional evolution of seaweed patterns, starting from a polycrystalline seed. To rule out

modeling artifacts that might influence the simulated morphological evolution, the solid-melt interfacial energy is assumed to be isotropic. This assumption idealizes grain boundaries observed in organic plastic polycrystals of SCN-based alloys, the interfacial energies of which are actually weakly anisotropic. The two-dimensional evolution of the solid-liquid interface simulated using the multicomponent multiphase-field model outlined in sect. 3 is shown in fig. 4(a). Here, the isolines that are plotted at intermittent timesteps correspond to where the phase indicator = 0.5. Initial stages of evolution depict an advancement of the solid-liquid interface followed by formation of a GBG. As the surface evolves, morphological instability sets in with increasing rapidity, which is indicated by the formation of bumps on either side of the GBG that bulge and extend into the melt. Both bumps amplify with time, and invaginate, forming an initial seaweed-like pattern. Given that the interfacial energy has been assumed to be isotropic, the pattern formation is mirror symmetric, indicating, as expected, a lack of any growth competition between the right and left patterns.

Isotropic pattern evolution simulated in 2-D was also observed in 3-D, where protuberances formed adjacent to grain boundaries and triple points were observed to amplify, as shown in fig. 4(b). The primary advantage of 3-D simulations over 2-D is that the former allows us to distinguish between the morphological evolution occurring adjacent to the triple points with respect to the grain boundaries. Our phase-field simulations corroborate the proposition of Schaefer and Glicksman [4], who observed that protuberances first appear near triple points and extend outwards, subsequently forming grain boundary ridges. 3-D bumps bulge further out into the melt more rapidly when compared to the morphological evolution rate of the 2-D ridges. As both structures amplify, weak parallel secondary ridges were developed, reminiscent of the surface rippling observed in our prior study [8]. Finally, the bumps and ridges that extend out into the melt invaginate, forming a forked hexagonal array of a seaweed-like microstructure.

The pattern continues to evolve into the melt without any signs of growth competition occurring among the instabilities arising from distinct seed grains. Overlapping trends in fig. 5(a) that show the temporal evolution of grain volume fractions corroborate isotropic characteristics of the simulated seaweed microstructure.

5.2 Influence of seed topology

Here, we examined the influence of seed topology on the pattern growth competition by altering the structural symmetry of the seed that was considered in sect. 5.1. To do so, contact angles between grains were chosen to be distinct, as shown in fig. 5(a). The resulting heights of grains 1–4 that ensured equal grain volume fractions were $15\Delta x$, $30\Delta x$, $23\Delta x$, and $15\Delta x$, respectively. Such an undulation of seed topology which is in contact with the supercooled melt was observed to induce a growth competition amongst the evolving seaweed patterns that amplified

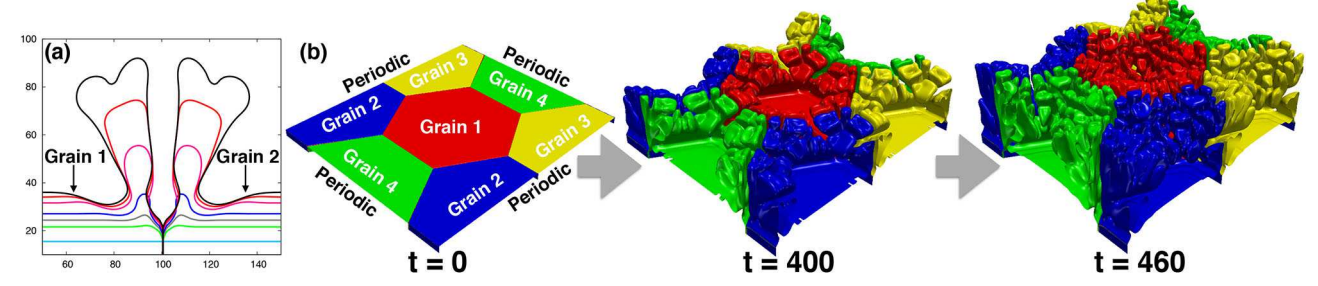


Fig. 4. (a) Contour plots ($\phi = 0.5$) showing the temporal evolution of seaweed patterns during columnar solidification solved over a 2-D computational domain. During the initial stages, the grooves formed at the grain triple-junction assist the autogenous interface fields to overcome the energy barrier required to drive the growth of perturbations. (b) Dynamic frames illustrating the evolving finger patterns starting from a 3-D polycrystalline setting (4 grains). The surface energy is assumed to be isotropic in both cases.

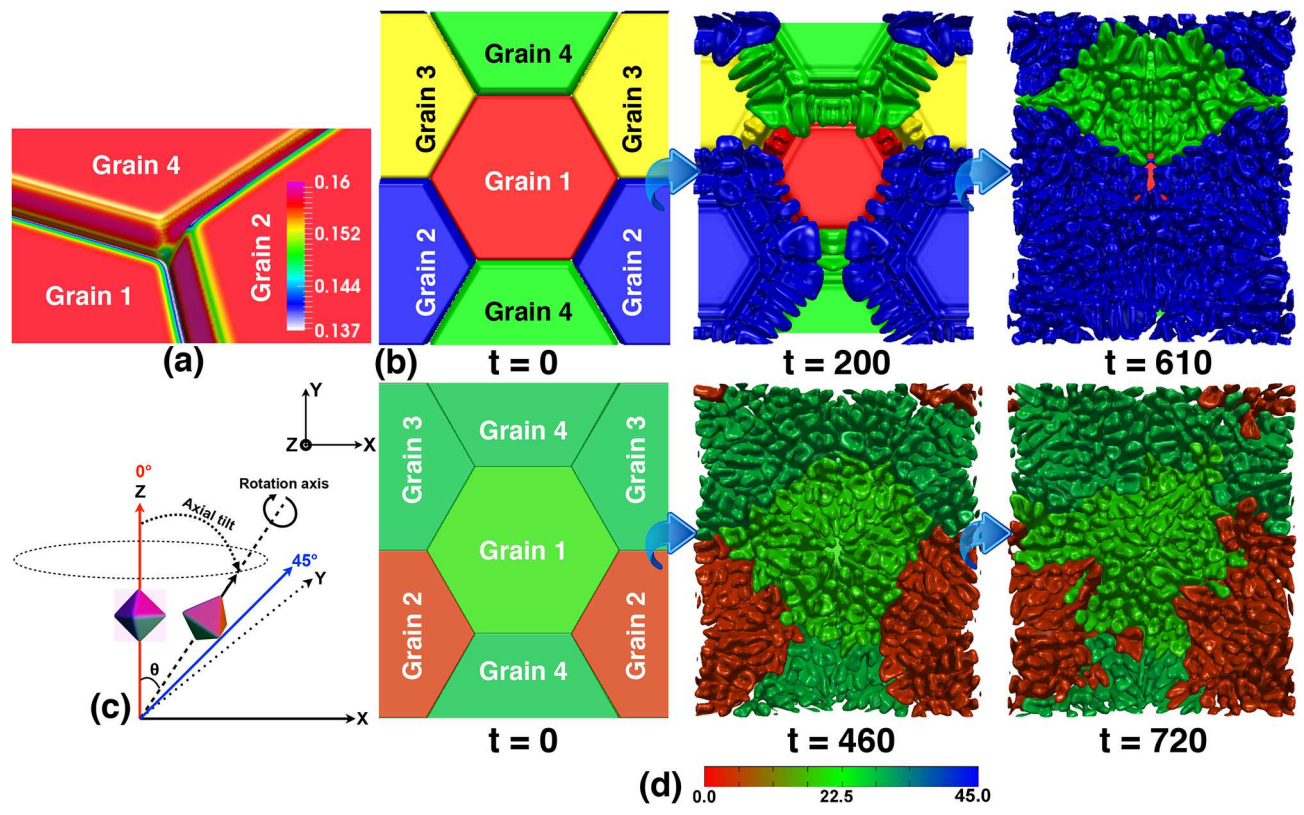


Fig. 5. (a) Magnified view of the polycrystalline setting with prescribed contact angles (70° between grains 1 and 2 and 56° between grains 1 and 4). The legend refers to the local curvature gradients. (b) Dynamic frames showing growth competition and asymmetric pattern formation due to the choice of contact angles illustrated in fig. 4(a). The surface energy is assumed to be isotropic. (c) Schematic diagram to illustrate pattern misorientation with respect to the most-preferred-orientation (along z-axis). (d) Dynamic frames showing growth competition and asymmetric pattern formation due to prescribed weak four-fold anisotropy in the surface energy (of the form $a_0\{1+\delta\cos(4\theta)\}$, where $\delta=0.001$). The contact angles between the grains are all assumed to be equal to 0°. The color-map illustrated underneath indexes the misorientation with respect to the z-axis.

from every grain, as shown in fig. 5(a). Grains 2 and 3 competed strongly with each other, whereas 1 and 4 were outgrown. The growth competition is evident from the plot in fig. 6(b), where the temporal volume fraction is found to be directly dependent on the initial height of the grain surface. Grains with equal initial heights did not compete with each other while the taller ones outgrew them.

5.3 Influence of misorientation

The anisotropy of the surface energy, even if weak, can have a significant influence on the morphological evolution of solidification patterns. Here, we simulated the anisotropic growth of seaweed patterns starting from the same 3D arrangement that corresponds to t=0 in

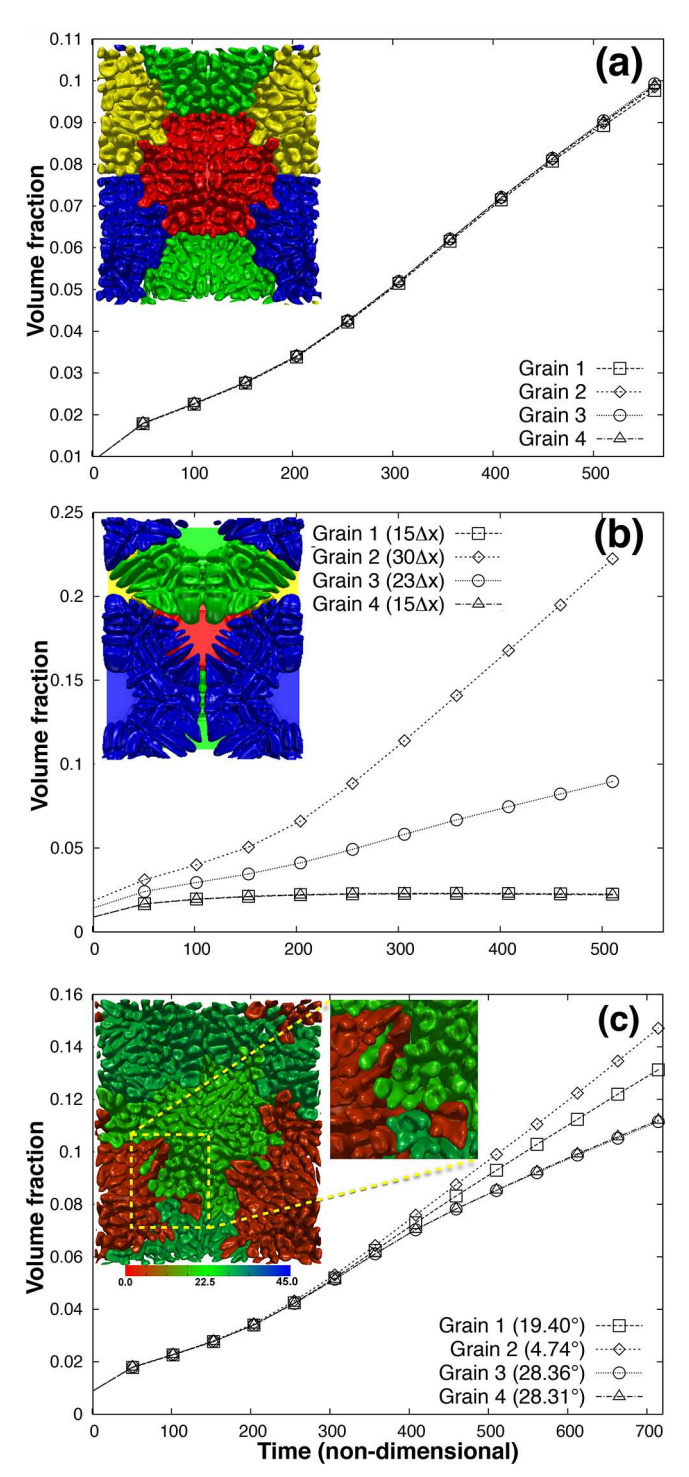


Fig. 6. Volume fractions plotted as a function of time for (a) symmetric (fig. 4) and (b) asymmetric pattern formation (fig. 5(b)) assuming surface energies to be isotropic. For the latter case, the pattern symmetry is broken due to non-equal contact angles in the initial polycrystalline setting shown in fig. 5(a). (c) On assuming weakly anisotropic surface energies and repeating the 3-D simulations, it is found that the growth competition during intermittent stages of evolution (due to relative misorientation) breaks the pattern symmetry (fig. 4(d)). The right inlet picture shows an instance where growth competition resulted in composite patterns.

fig. 4 by selecting a fourfold crystalline anisotropy (see fig. 5(c)). Relative misorientation is defined as the axial tilt with respect to the surface normal of the initial flat seed that points into the melt. To understand the influence of relative misorientation on the growth competition, the anisotropy strength δ is chosen to be 0.001. The polycrystalline seed that comprises grains 1, 2, 3 and 4 is assigned axial tilts of 19.40°, 4.74°, 28.36° and 28.31°, respectively, while the crystalline rotation about the tilted axes is assigned randomly with prior knowledge from our previous findings that it does not impact the growth competition.

A significant growth competition is observed in the evolving seaweed pattern as shown in fig. 5(d). We observe that the most favorably oriented, i.e. grain 2 outgrows misoriented neighbors. This overgrowth is analyzed in fig. 6(c) where the volume fraction of grains 1 and 2 is seen to temporally diverge with respect to that of 3 and 4. However, temporal volume fractions of grains 3 and 4 nearly overlap as their relative misorientation is small. Growth competition of faceted crystals modeled in our earlier work is characterized by overgrowths where the misoriented crystal ceases to grow in a direction normal to the seed surface. However, an additional mode of growth competition is observed in the present simulations; where fingers emerging from the morphological instability of grain 1, colored red in fig. 6(c), infiltrate into pore spaces belonging to neighboring grains as seen in the inset. It is worth noting that this alternate mode of growth competition fingers of favorably oriented grains which compete along a lateral direction via intertwining has never been reported in the context of columnar solidification earlier.

5.4 Influence of fluid convection

Phase-field simulations described in the previous sections clearly show that seaweed patterns of materials with isotropic surface energies do not compete while any growth competition can be attributed to the anisotropy of surface energy or the non-uniformity of seed topology. In the present section, we investigate the influence of fluid convection on the evolution of seaweed patterns emerging from the initial bi-crystalline configuration shown in fig. 4(a). The presence of 3-D fluid flow pathways can influence the alignment of surface ripples during the early stages of columnar solidification, as shown in fig. 7. This provides a strong basis for analyzing late stage growth competition of such microstructures. For this study, we choose a shifting computational domain [49] comprised of 1000×1000 grid-points. The simulated seaweed patterns corresponding to different flow intensities ranging from Re = 1 to 300 are compared in fig. 8. While the seaweed pattern emerging in upstream, i.e. the left region closer to the inflow, is seen to predominate at Re = 1, this trend is reversed as the value of Re is increased. For $Re \in (10, 100)$, the seaweed pattern emerging from the right crystal in downstream dominates the growth process. Irrespective of the observed growth competition, the initial instabilities that evolve in the melt can be best described as degenerate seaweeds. At larger flow intensities (Re > 300), the growth competition ceases and a characteristic tilt in

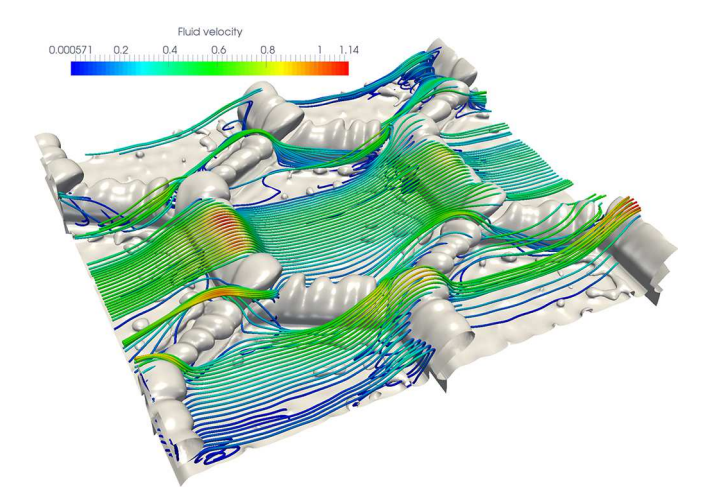


Fig. 7. Formation of surface ripples [4] at grain boundaries of an impure SCN-based alloy embedded in its supersaturate melt, simulated using the model outlined in sect. 3. Extending the previous work of the authors [8], which was limited to the diffusion-limited regime, including the effects of melt convection shows its strong influence on ripple alignment. The three-dimensional nature of the flow field allows it to curl around the solid-liquid interface.

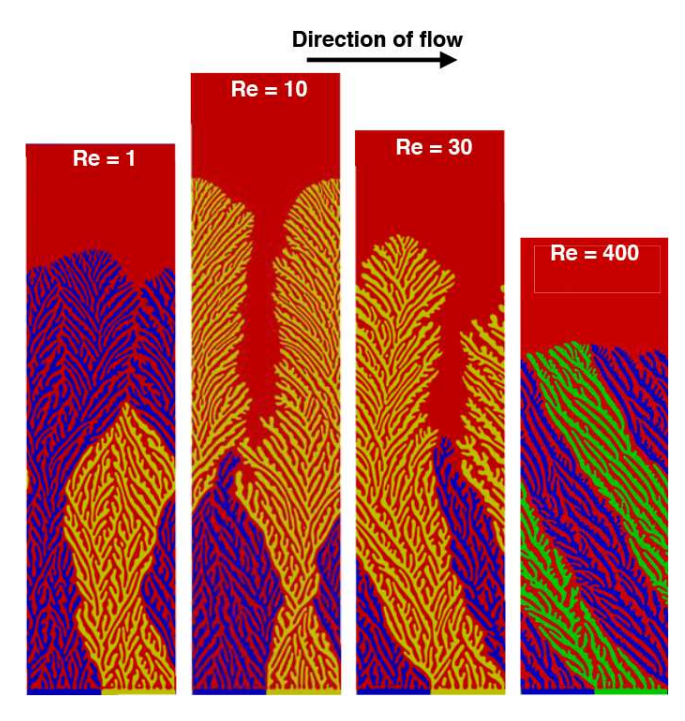


Fig. 8. Phase-field simulations of the seaweed patterns corresponding at different flow intensities. The surface energy has been assumed to be isotropic while the initial arrangement of grains corresponds to fig. 4(a). Simulations were performed in a moving frame of reference as described in our previous work [49], where the sliding occurred at z=1000. The Neumann boundary condition is applied for μ at z=1000. An initialized and a fully developed flow with a velocity u is introduced in the x-direction, along with the periodic boundary conditions at x=0 and x=1000.

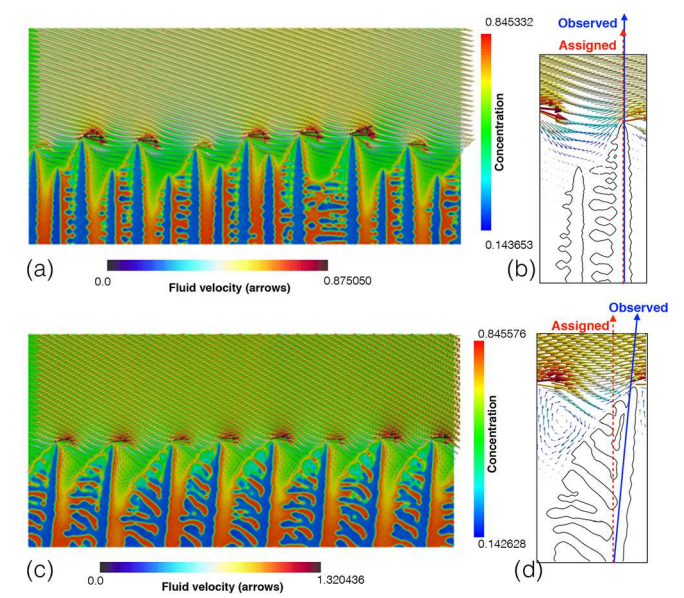


Fig. 9. Phase-field simulations of the columnar solidification microstructures corresponding to (a) Re=100, $\delta_{\alpha\beta}=0.1$ and (c) Re=400, $\delta_{\alpha\beta}=0.06$. Panels (b) and (d) represent the magnified view of (a) and (c), respectively, where phase-field contours are plotted along with flow vectors. Pronounced extension of sidebranches towards upstream is observed in both the cases *i.e.* (a) and (c), that is reminiscent of earlier numerical findings [50]. In (d), vortices are more pronounced as compared to (b) for a stronger convective flow. Tilting of primary stems towards downstream is also observed in (c) while upstream sidebranches appear to be isotropic.

the seaweed pattern, opposite to the flow direction, is observed. It is worth mentioning at this point that seaweed patterns are typically known to evolve isotropically, however, for the first time, our simulation results show that growth competition in crystals with low surface energies can be induced via fluid convection. A detailed analysis of the observed convection-mediated growth competition in seaweed patterns has recently been reported [42].

As opposed to the influence of convection on isotropically evolving seaweed patterns, there have been a number of studies on the convection-mediated tilting of dendrites. In fig. 9, we illustrate the competition arising between the surface tension and flow intensity that manifests as tilting of the primary stem. At a moderate flow intensity (Re = 100) and anisotropy strength, $\delta = 0.1$ (fig. 9(a)), the primary stem stays aligned with the growth direction while sidebranches evolve opposite to the flow direction. The simulated flow vectors plotted in fig. 9(b) are found to glide over the surface as they sweep the domain. On the contrary, when Re = 400 and $\delta = 0.06$ (fig. 9(c)), a significant tilt in the primary stem is observed. In the latter, the simulated flow vectors plotted in fig. 9(d) are found to curl as they impact the sidebranches. It is to be noted that tilting of the primary stem results in misorientation of the dendrites with respect to the assigned four-fold anisotropy of the surface energy. As an outcome of this tilt, the misoriented sidebranches evolve isotropically with a seaweed-like morphology.

6 Conclusions

In the present study, we have analyzed the various factors that can induce growth competition in columnar solidification of weakly anisotropic microstructures using multiphase-field simulations. The convective term, which is incorporated in the grand chemical potential of Choudhury and Nestler [31] by adopting the approach of Beckermann et al. [27], was validated by computing and comparing drag coefficients at different Reynolds numbers with theory. The triple-point angles corresponding to static grain boundary grooves simulated using the numerical approach are found to be in agreement with Young's law. In one of our earlier works [8], the morphological instability adjacent to the grain boundary groove and surface break down was investigated for conditions pertaining to columnar solidification. Here, we have extended our numerical studies to investigate the growth competition and the ensuing pattern formation for crystals with low capillary anisotropy strengths. The adopted multiphase-field approach, where every grain is assigned a unique phasefield order parameter, facilitates the analysis of growth competition as any temporal changes in grain volume fraction can easily be tracked.

In the absence of melt convection and capillary anisotropy, seaweed patterns arising due to morphological instability of symmetric GBGs, evolve isotropically with mirror symmetry, or in other words, the final microstructure shows no imprints of growth competition. However, if the seed topology is undulated, grain contact angles change leading to the formation of asymmetric grooves. The seaweed patterns that evolve compete with one another as indicated by temporally diverging volume fraction plotted for different grains (fig. 6(b)). Therefore, our simulations suggest that initial conditions, particularly the seed morphology, can significantly influence the growth competition in isotropic solidification patterns. Similarly, if the surface energy is assumed to be anisotropic, it is observed that relative misorientation among grains can induce growth competition in the seaweed patterns that originate from the breakdown of polycrystalline seed surface. Since the evolving seaweed pattern shows strong tendencies to inter-penetrate neighboring ones, overgrowth occurs along the growth axis in addition to the lateral directions.

Starting from a uniform seed morphology which is free of any undulations, convective flow is shown to induce growth competition in seaweed patterns even if surface energy is isotropic. Whether or not, the evolving seaweed patterns compete is found to be strongly dependent on flow intensity quantified by Reynolds number (Re). At a small flow intensity (Re=1), the grain in the upstream outgrows its neighbor. However, at moderate flow intensities $(10 \le Re \le 100)$, the trend is found to be reversed. At a large flow intensity, the growth competition ceases and seaweed patterns are characterized by a unique tilt angle. To the best of our knowledge, our simulations for the first time show the mechanism of convection-mediated growth competition in seaweed patterns. The dependence of the observed growth competition in solidification mi-

crostructures on flow intensity is of fundamental interest; the growth competition ceases at larger Re and the pattern is characterized by a tilt.

Although the present work provides basic insights into the instabilities originating at GBGs and exposes the mechanisms by which weakly anisotropic solidifying patterns can compete, it needs to be extended to explore how a three-dimensional characteristic of melt convection influences this behavior. Moreover, our studies are limited to laminar flow as the influence of melt turbulence (i.e. Re > 5000) on the morphological evolution of seaweed structures has not been considered. Finally, it remains interesting to analyze the interaction of melt convection on capillary-mediated bias-fields, now known to reside on solid-liquid interfaces [51–53].

This material is based upon research supported by the National Aeronautics and Space Administration (NASA) through Contract No. 80NSSC18K1440 and the National Science Foundation (NSF) under Grant No. 1763128. The author acknowledges preliminary discussions with former colleagues at KIT, Pavan L. Veluvali and Michael Selzer. One of the authors (MEG) acknowledges his partial support provided by the Allen S. Henry Chair, Florida Institute of Technology.

Author contribution statement

Both authors were involved in the preparation of this manuscript, and have read and approved the final manuscript.

Publisher's Note The EPJ Publishers remain neutral with regard to jurisdictional claims in published maps and institutional affiliations.

References

- 1. W.W. Mullins, R. Sekerka, J. Appl. Phys. 35, 444 (1964).
- N. Noël, H. Jamgotchian, B. Billia, J. Cryst. Growth 181, 117 (1997).
- H. Xing, C. Wang, J. Wang, C. Chen, Sci. China Phys. Mech. 54, 2174 (2011).
- 4. R. Schaefer, M. Glicksman, Metall. Trans. 1, 1973 (1970).
- N. Noël, H. Jamgotchian, B. Billia, J. Cryst. Growth 187, 516 (1998).
- D. Benielli, N. Bergeon, H. Jamgotchian, B. Billia, P. Voge, Phys. Rev. E 65, 051604 (2002).
- K. Murakami, H. Aihara, T. Okamoto, Acta Metall. Mater. 32, 933 (1984).
- K. Ankit, H. Xing, M. Selzer, B. Nestler, M.E. Glicksman, J. Cryst. Growth 457, 52 (2017).
- 9. D. Tourret, A. Karma, Acta Mater. 82, 64 (2015).
- H. Jamgotchian, N. Bergeon, D. Benielli, P. Voge, B. Billia,
 R. Guérin, Phys. Rev. Lett. 87, 166105 (2001).
- 11. Y.J. Chen, S.H. Davis, J. Fluid Mech. 421, 369 (2000).
- 12. J. Nittmann, H.E. Stanley, Nature 321, 663 (1986).
- E. Ben-Jacob, G. Deutscher, P. Garik, N.D. Goldenfeld, Y. Lareah, Phys. Rev. Lett. 57, 1903 (1986).

- B. Utter, R. Ragnarsson, E. Bodenschatz, Phys. Rev. Lett. 86, 4604 (2001).
- 15. B. Utter, E. Bodenschatz, Phys. Rev. E 66, 051604 (2002).
- 16. B. Utter, E. Bodenschatz, Phys. Rev. E 72, 011601 (2005).
- T. Ihle, H. Müller-Krumbhaar, Phys. Rev. E 49, 2972 (1994).
- S. Akamatsu, G. Faivre, T. Ihle, Phys. Rev. E 51, 4751 (1995).
- J. Dantzig, P. Di Napoli, J. Friedli, M. Rappaz, Metall. Mater. Trans. A 44, 5532 (2013).
- W.J. Boettinger, S.R. Coriell, A. Greer, A. Karma, W. Kurz, M. Rappaz, R. Trivedi, Acta Mater. 48, 43 (2000).
- X. Tong, C. Beckermann, A. Karma, Q. Li, Phys. Rev. E 63, 061601 (2001).
- W.J. Boettinger, J.A. Warren, C. Beckermann, A. Karma, Annu. Rev. Mater. Res. 32, 163 (2002).
- N. Provatas, Q. Wang, M. Haataja, M. Grant, Phys. Rev. Lett. 91, 155502 (2003).
- M. Amoorezaei, S. Gurevich, N. Provatas, Acta Mater. 60, 657 (2012).
- A. Choudhury, M. Kellner, B. Nestler, Curr. Opin. Solid State Mater. Sci. 19, 287 (2015).
- H. Xing, K. Ankit, X. Dong, H. Chen, K. Jin, Int. J. Heat Mass Transfer 117, 1107 (2018).
- C. Beckermann, H.J. Diepers, I. Steinbach, A. Karma, X. Tong, J. Comput. Phys. 154, 468 (1999).
- C. Chen, Y. Tsai, C. Lan, Int. J. Heat Mass Transfer 52, 1158 (2009).
- B. Nestler, A.A. Wheeler, L. Ratke, C. Stöcker, Phys. D: Nonlinear Phenom. 141, 133 (2000).
- W. Boettinger, F. Biancaniello, S. Coriell, Metall. Trans. A 12, 321 (1981).
- 31. A. Choudhury, B. Nestler, Phys. Rev. E 85, 021602 (2012).
- B. Nestler, H. Garcke, B. Stinner, Phys. Rev. E 71, 041609 (2005).

- 33. N. Moelans, Acta Mater. 59, 1077 (2011).
- H. Xing, X. Dong, H. Wu, G. Hao, J. Wang, C. Chen, K. Jin, Sci. Rep. 6, 26625 (2016).
- 35. Y. Chen, B. Billia, D.Z. Li, H. Nguyen-Thi, N.M. Xiao, A.A. Bogno, Acta Mater. **66**, 219 (2014).
- J. Hötzer, O. Tschukin, M.B. Said, M. Berghoff, M. Jainta,
 G. Barthelemy, N. Smorchkov, D. Schneider, M. Selzer, B.
 Nestler, J. Mater. Sci. 51, 1788 (2016).
- 37. A. Karma, Phys. Rev. E 48, 3441 (1993).
- 38. A. Karma, W.J. Rappel, Phys. Rev. E 60, 3614 (1999).
- 39. G. Marsaglia, T.A. Bray, SIAM Rev. 6, 260 (1964).
- Y. Lu, C. Beckermann, J.C. Ramirez, J. Cryst. Growth 280, 320 (2005).
- 41. M. Selzer, PhD Thesis, KIT-Bibliothek (2014).
- V. Laxmipathy, F. Wang, M. Selzer, B. Nestler, K. Ankit, Comput. Mater. Sci. 170, 109196 (2019).
- 43. M. Griebel, T. Dornseifer, T. Neunhoeffer, Numerical Simulation in Fluid Dynamics: A Practical Introduction (Society for Industrial and Applied Mathematics, 1998).
- 44. J.A. Warren, R. Kobayashi, A.E. Lobkovsky, W.C. Carter, Acta Mater. **51**, 6035 (2003).
- 45. S. Yeh, C. Chen, C. Lan, J. Cryst. Growth 324, 296 (2011).
- W. Mullins, Trans. Am. Inst. Min. Metall. Eng. 218, 354 (1960).
- 47. H. Schlichting, K. Gersten, Boundary-Layer Theory (Springer, 2016).
- 48. D.J. Tritton, J. Fluid Mech. 6, 547 (1959).
- K. Ankit, A. Choudhury, C. Qin, S. Schulz, M. McDaniel,
 B. Nestler, Acta Mater. 61, 4245 (2013).
- R. Tönhardt, G. Amberg, J. Cryst. Growth 213, 161 (2000).
- 51. M. Glicksman, K. Ankit, Metals 7, 547 (2017).
- 52. M. Glicksman, K. Ankit, J. Mater. Sci. **53**, 10955 (2018).
- M. Glicksman, K. Ankit, IOP Conf. Ser.: Mater. Sci. Eng. 529, 012027 (2019).